Report

Current Biology

In Vitro Reconstitution of Dynein Force Exertion in a Bulk Viscous Medium

Graphical Abstract

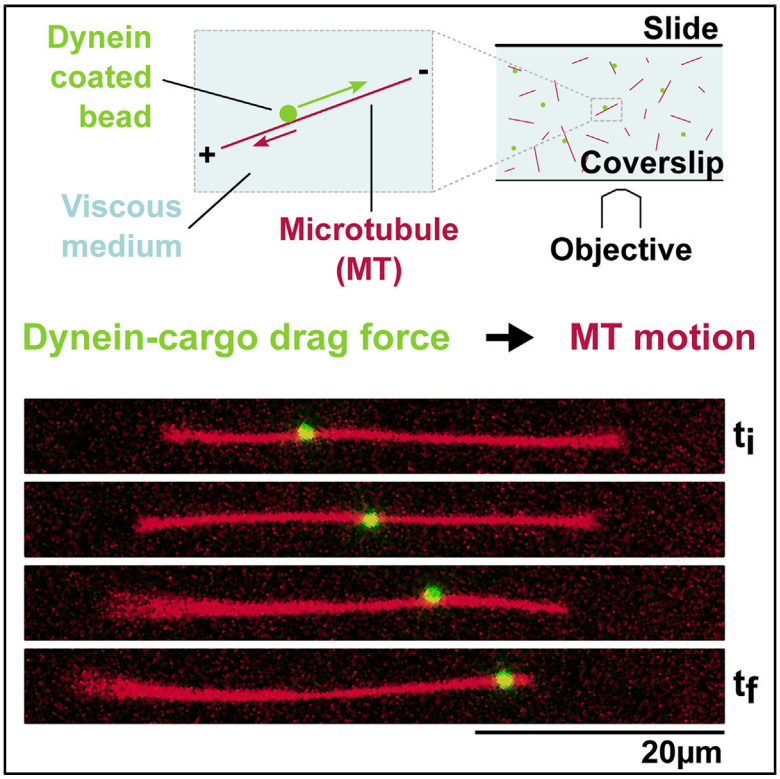

Authors

Héliciane Palenzuela, Benjamin Lacroix, Jérémy Sallé, ..., Antoine Jegou, Guillaume Romet-Lemonne, Nicolas Minc

Correspondence

romet@ijm.fr (G.R.-L.), nicolas.minc@ijm.fr (N.M.)

In Brief

By developing a bulk motility assay, Palenzuela et al. demonstrate that the sole motion of dynein-driven cargos in a viscous solution can generate pulling forces that move microtubules in the direction opposite to the cargo's. These data provide key support for dynein pulling in bulk cytoplasm as an important mode of cytoskeleton force exertion.

Highlights

- A bulk motility assay reconstitutes dynein pulling microtubules in the cytoplasm
- A single motile cargo in a viscous solution generates near pN forces on a microtubule
- Forces are additive, recapitulating a length-dependent model
- Tug-of-war situations yield centration of minimal asters in bulk

Palenzuela et al., 2020, Current Biology *30*, 4534–4540
November 16, 2020
https://doi.org/10.1016/j.cub.2020.08.078

CellPress

CellPress

Current Biology

Report

In Vitro Reconstitution of Dynein Force Exertion in a Bulk Viscous Medium

Héliciane Palenzuela,[1] Benjamin Lacroix,[1] Jérémy Sallé,[1] Katsuhiko Minami,[2] Tomohiro Shima,[2] Antoine Jegou,[1] Guillaume Romet-Lemonne,[1,*] and Nicolas Minc[1,3,*]

[1]Institut Jacques Monod, Université de Paris, CNRS, 75006 Paris, France

[2]Graduate School of Science, The University of Tokyo, 113-0033 Tokyo, Japan

[3]Lead Contact

*Correspondence: romet@ijm.fr (G.R.-L.), nicolas.minc@ijm.fr (N.M.)

https://doi.org/10.1016/j.cub.2020.08.078

SUMMARY

The forces generated by microtubules (MTs) and their associated motors orchestrate essential cellular processes ranging from vesicular trafficking to centrosome positioning [1, 2]. To date, most studies have focused on MT force exertion by motors anchored to a static surface, such as the cell cortex *in vivo* or glass surfaces *in vitro* [2–4]. However, motors also transport large cargos and endomembrane networks, whose hydrodynamic interactions with the viscous cytoplasm should generate sizable forces in bulk. Such forces may contribute to MT aster centration, organization, and orientation [5–14] but have yet to be evidenced and studied in a minimal reconstituted system. By developing a bulk motility assay, based on stabilized MTs and dynein-coated beads freely floating in a viscous medium away from any surface, we demonstrate that the motion of a cargo exerts a pulling force on the MT and propels it in opposite direction. Quantification of resulting MT movements for different motors, motor velocities, over a range of cargo sizes and medium viscosities shows that the efficiency of this mechanism is primarily determined by cargo size and MT length. Forces exerted by cargos are additive, allowing us to recapitulate tug-of-war situations or bi-dimensional motions of minimal asters. These data also reveal unappreciated effects of the nature of viscous crowders and hydrodynamic interactions between cargos and MTs, likely relevant to understand this mode of force exertion in living cells. This study reinforces the notion that endomembrane transport can exert significant forces on MTs.

RESULTS

A Bulk Motility Assay to Study Dynein Force Exertion in Bulk

Multiple *in vivo* studies have suggested that cytoplasmic dynein may exert pulling forces on microtubules (MTs) directly from bulk cytoplasm, without contacting the cortex [12]. This mode of force exertion may have a prevalent function in many cells, as it is thought to naturally arise from motor-driven transport of vesicles, organelles, and larger endomembrane networks in the viscous cytoplasm. Such forces have, for instance, been predicted to contribute to the outward transport of MTs that have been released from centrosomes, potentially promoting aster expansion and organization [10, 11, 15]. They may also apply a net force to asters and cause them to move, when MTs are connected to the centrosome, with no requirement for MTs to contact the cell surface [12, 16, 17]. Because longer MTs could accumulate more cargos, such pulling forces have been proposed to increase with MT length, providing a shape-sensing design for aster centration and orientation in large eggs and early blastomeres [7–9, 18]. Simple theoretical considerations suggest that a cargo moving in bulk is akin to a micro-swimmer, generating a hydrodynamic drag force scaled to its speed, size, and cytoplasm viscosity [6, 19]. To date, however, the lack of minimal reconstitution of dynein bulk pulling has hampered deciphering the basic designs of this essential mode of MT force exertion, its general relevance, and its limitations.

In vitro surface motility assays based on motors attached to a coverslip have populated the cytoskeleton literature in recent years, delineating essential principles of force generation in cells [2]. We designed a bulk motility assay to study how an object transported along a MT in a viscous medium, away from any fixed anchoring point, may create forces on the MTs and cause MT movement. Taxol-stabilized and fluorescently labeled MTs were mixed with dynein-coated fluorescent beads in a viscous medium, supplemented with ATP, and flowed into a microscopy chamber (Figure 1A; STAR Methods) [20]. The motor domain of *Dictyostelium discoideum* cytoplasmic dynein was biotinylated *in vivo* and then purified [21, 22]. The dynein molecules were bound to streptavidin beads through their biotin moiety. Prior to each assay, dynein activity was quantified by performing standard MT gliding assays, where we monitored the movement of MTs on dynein-coated coverslips and on carpets of surface-anchored, dynein-coated beads (Figures S1A–S1C; STAR Methods). During assay optimization, we considered using different viscous agents and selected methylcellulose (MC), because other commonly used crowders tended to over-bundle MTs and/or strongly affect dynein activity (Figures S1D and S1E) [23, 24]. The range of MC concentrations was determined to

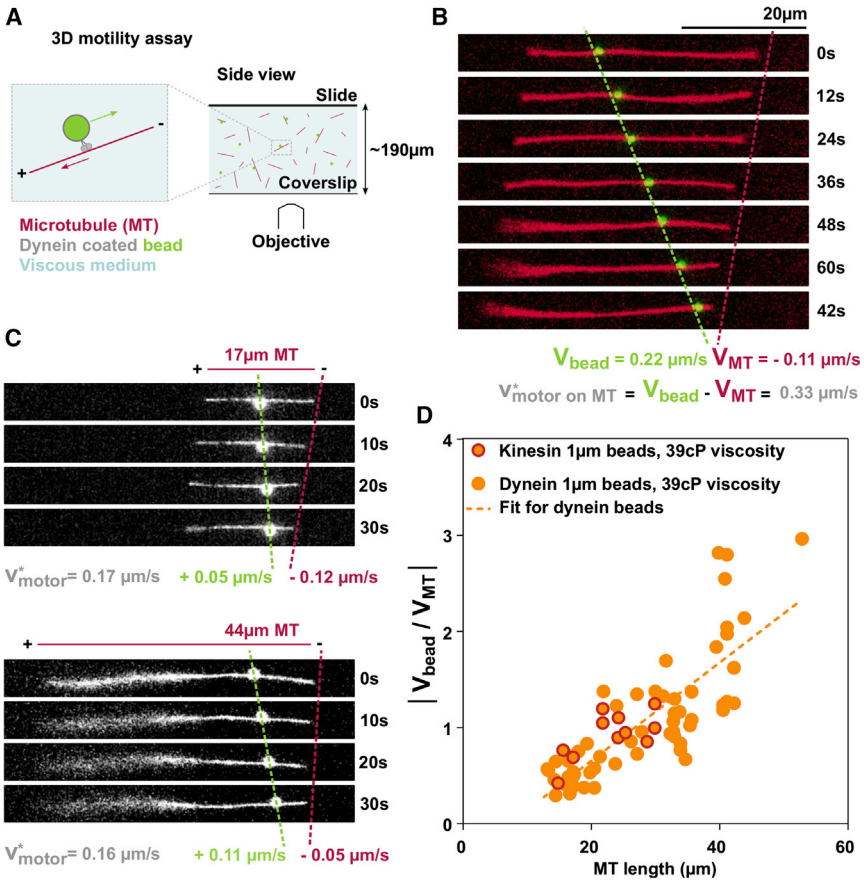

Figure 1. A Bulk Motility Assay Reconstituting Dynein Pulling on MTs in Bulk

(A) Sketch representing the bulk motility assay. Taxol-stabilized MTs and dynein-coated beads are mixed and flowed in a microscopy chamber, which is sealed with VALAP (STAR Methods). MTs and beads can freely meet, and the subsequent bead gliding is recorded.

(B) Time lapse of a 0.5-µm-diameter, dynein-coated bead gliding on a MT. The motor velocity on the MT is equal to the difference between the bead velocity and the MT velocity in the lab referential.

(C) Time lapse of a 1-µm-diameter, dynein-coated bead gliding on a short (17 µm) or a long (44 µm) MT. For a similar motor velocity, the shorter MT is displaced faster.

(D) Bead-to-MT speed ratio as a function of the MT length for 1-µm diameter dynein- or kinesin-coated beads in a 1.18% methylcellulose (MC) viscous medium (measured viscosity: 39 cP; dynein beads: n = 57, 9 independent experiments, three protein batches; kinesin beads: n = 11, 4 independent experiments, one protein batch).

See also Figure S1 and Video S1.

ensure reproducible pipetting and chamber loading, while limiting MT and bead sedimentation, and also to test the influence of medium viscosity on bulk forces (see hereafter). Given these considerations, each assay allowed to capture in general ~5 events of bead gliding during a period of ~1 h, after which most beads had reached the minus end of MTs, where they remained bound.

At chamber mid-height, several tens of micrometers away from either chamber coverslip surface, MTs that appeared horizontal and to which a dynein-coated bead had bound were immediately imaged by time-lapse fluorescent microscopy. Remarkably, the sole motion of a dynein-coated bead 0.5 µm in diameter along a MT of ~30 µm in length, in a viscous medium, was sufficient to cause a concomitant marked steady MT movement in the opposite direction in the microscope frame of reference (Figure 1B; Video S1). Tracking both bead and MT end positions revealed that, in the majority of cases, cargo moved at near-constant speeds, causing a resultant constant MT speed, and that both motions immediately stopped once the cargo reached the MT minus end (Figures S1F and S1G). We also noticed events in which the cargo moved and then stopped before reaching the end of the MT. These arrests presumably reflected the detachment or stalling of motors carrying the beads. Yet, in such events, the MT also moved concomitantly and in opposite direction with the cargo and stopped when the cargo stopped. We conclude that dynein-driven cargo motion in bulk is sufficient to pull and displace MTs.

Taxol-stabilized MTs typically ranged from 10 to 50 µm in length. We noticed that beads with the same size moving at similar speeds on a short versus a long MT tended to displace the short MT significantly faster than the long one (Figures 1C, 1D, and S2A). Accordingly, by computing the net velocity of the beads, V_{bead}, and of the MT, V_{MT}, with respect to the surrounding fluid (i.e., in the microscope frame of reference), we found that the speed ratio $|V_{bead} / V_{MT}|$ increased with MT length in a near-linear manner (correlation coefficient, R = 0.80; linear fit, $R^2 = 0.64$; Figure 1D). Importantly, even though the net velocity of dynein-coated beads along MTs exhibited some variability, likely reflecting the number of motors engaged between the bead and the MT, it did not significantly affect the dependence of the bead-to-MT speed ratio on MT length. Accordingly, faster-moving beads, obtained by incubation with much higher dynein concentrations, also behaved the same (Figures S2B and S2C). In addition, this behavior was also unaffected when using kinesin-coated beads, with reversed polarity and net velocity on MTs (Figures 1D and S2D). Finally, this trend was also mostly similar in single versus small MT bundles of 2 to 3 MTs, suggesting that MT length and not radius was the most relevant parameter dictating MT motion in response to cargo bulk force (Figure S2E). These data are consistent with the notion that bulk MT displacement, in response to a cargo viscous force, is determined by the MT's hydrodynamic drag coefficient that linearly scales with its length, with little influence from its diameter [2, 25, 26].

The Efficiency of MT Propulsion Depends on Cargo Size

An important aspect of bulk hydrodynamic forces is that they are predicted to increase with the cargo drag coefficient, which increases with cargo size [25]. We thus repeated the bulk motility assay in the same conditions but with beads of different

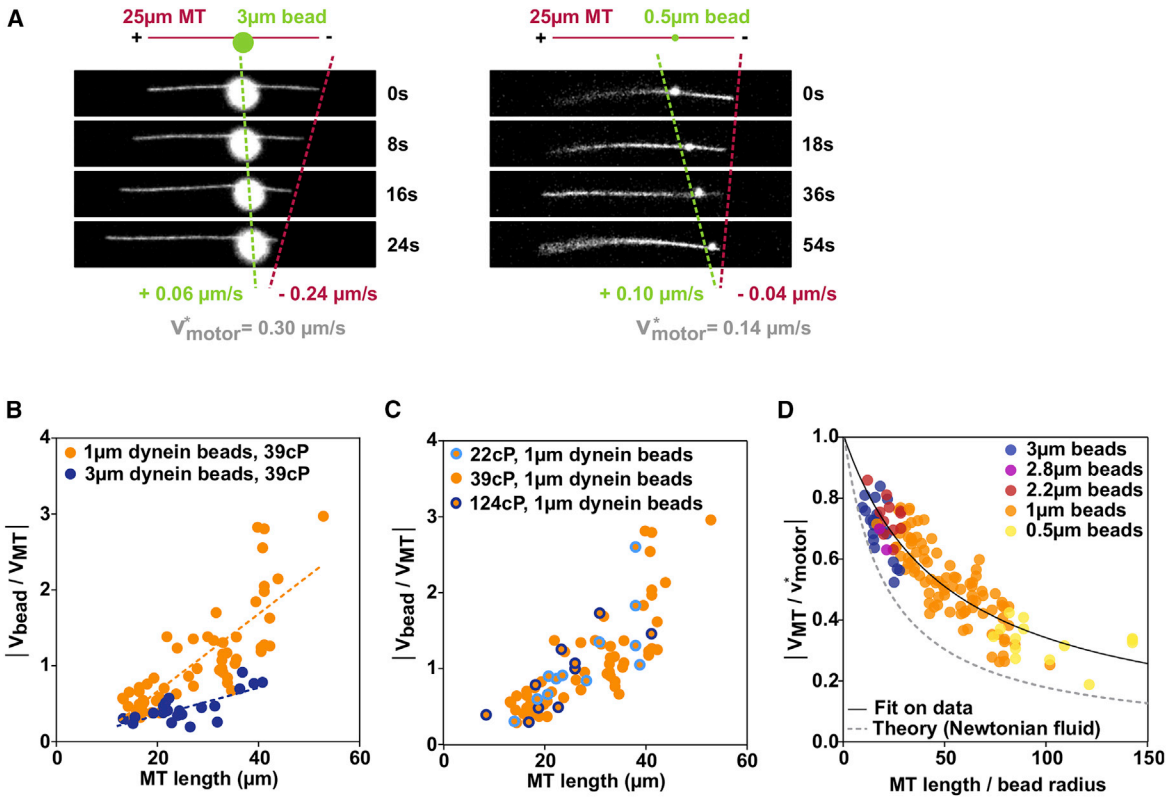

Figure 2. Impact of Cargo Size on MT Bulk Pulling Efficiency

(A) Time lapses of a 0.5- or 3-µm-diameter, dynein-coated bead gliding on an ~25-µm MT. For a similar MT length, the larger bead will displace the MT more than the smaller bead.

(B) Bead-to-MT speed ratio plotted as a function of MT length for dynein-coated beads of 1 µm and 3 µm diameter in a 39-cP MC viscous medium (1-µm beads: n = 57, 9 independent experiments, three protein batches; 3-µm beads: n = 21, 7 independent experiments, two protein batches). The dotted lines are linear fits.

(C) Bead-to-MT speed ratio plotted as a function of MT length for 1-µm-diameter, dynein-coated beads in a 0.85%, 1.18%, or 1.60% MC medium (respectively yielding measured viscosities of 22 cP, 39 cP, and 124 cP; 22 cP: n = 12, 3 independent experiments, one protein batch; 39 cP: n = 57, 9 independent experiments, three protein batches; 124 cP: n = 10, 5 independent experiments, two protein batches).

(D) MT-to-motor speed efficiency ratio plotted as a function of the ratio of MT length to bead radius for beads of diameters of 0.5, 1, 2.2, 2.8, and 3 µm in medium of viscosities of 22 cP, 39 cP, or 124 cP (0.5-µm beads: n = 14, 4 independent experiments, one protein batch; 1-µm beads: n = 79, 17 independent experiments, five protein batches; 2.2-µm beads: n = 11, 3 independent experiments, one protein batch; 2.8-µm beads: n = 2, 2 independent experiments, one protein batch; 3-µm beads: n = 21, 7 independent experiments, two protein batches). A fit of the data is shown as a black line and the theoretical behavior in a Newtonian fluid as a gray dashed line.

See also Figures S2 and S3 and Video S1.

diameters. As predicted, for a similar range of MT lengths, we found that larger beads caused a faster MT displacement than smaller beads (Figures 2A and 2B; Video S1). These results directly demonstrate that the motion of a cargo in bulk will drive a consequent MT displacement that respects a balance of hydrodynamic forces between the two objects, which behave as an isolated system, so that $|\gamma_{MT}{}^{*}V_{MT}| = |\gamma_{bead}{}^{*}V_{bead}|$, with γ the viscous drag coefficients. Importantly, because both drag coefficients are proportional to the medium viscosity, this parameter should not influence the bead-to-MT speed ratio. Accordingly, varying viscosity by changing the concentration of MC did not influence the bead-to-MT speed ratio (Figures 2C, S2F, and S2G). Thus, although viscosity will linearly influence the drag forces that motors will have to overcome, it has no influence on the speed ratio between the cargo and the MT. With the ranges of cargo size, motor velocity, and medium viscosity that we explored in our assays, we estimated based on Stokes's formula that individual mobile cargos applied to MTs a net bulk force ranging from 0.01 pN (small beads, moving slowly in low viscosity medium) up to 0.9 pN (larger beads, moving faster in higher viscosity). We note that this force computation may be prone to minor inaccuracy, because the presence of the MT may affect the fluid flow around the motile bead. These forces are sufficient to move MTs of tens of micrometers at typical speeds of few tenths of µm/s. In a cellular context, where several motors collectively move cargos of similar sizes at velocities of ~1 µm/s in a cytoplasm typically 100–1000× more viscous than water [27], the resulting forces are expected to be even higher, on the order of several pN, comparable to forces exerted by cortex-anchored motors [28, 29].

Because the extent of MT propulsion appeared to depend solely on MT length and bead diameter, we next sought to determine whether all our data followed a master curve, as a function of the MT-length-to-bead-radius ratio (L_{MT}/R_{bead}), which is a first-order approximation for the ratio of their viscous drag coefficients

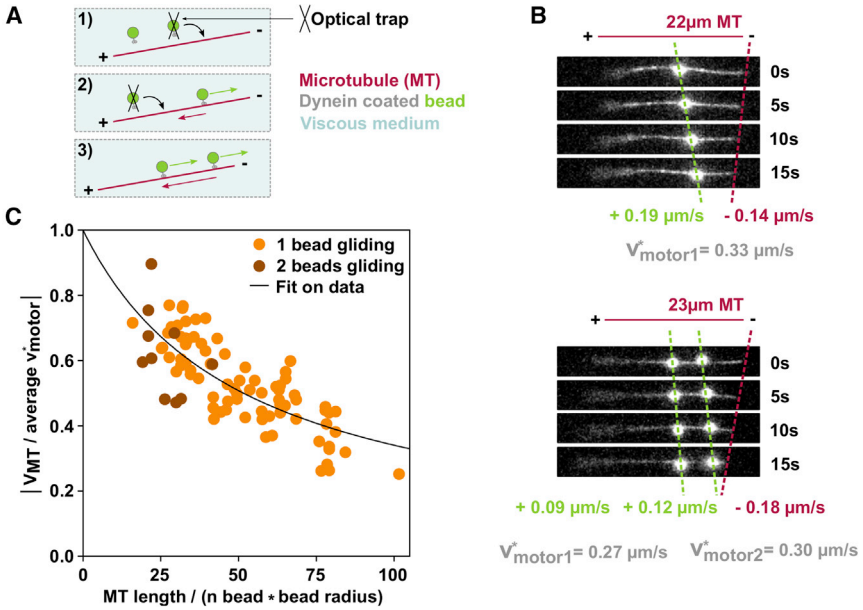

Figure 3. Collective Effect of Two Beads Pulling on a Single MT

(A) Sketch showing how two dynein-coated beads are placed on a MT using an optical trap to facilitate this assay.

(B) Time lapse of one or two beads walking on ~22-µm-long MTs. For similar motor velocities, the MT is displaced more when two beads are walking on it.

(C) MT-to-motor speed ratio plotted as a function of the ratio of the MT length to the bead number multiplied by the bead radius. Data shown are 1-µm-diameter beads, walking on MTs alone or by two away from each other, for beads coated with dynein or kinesin in a viscous medium of 22 cP, 39 cP, or 124 cP (1 bead gliding: n = 79, 17 independent experiments, five protein batches; 2 beads gliding: n = 10, 4 independent experiments, two protein batches). The fit on the data of all bead sizes is shown as a black line.

See also Figure S3 and Videos S2 and S3.

(Figure S3A; STAR Methods). For this, we computed an MT-to-motor speed ratio ($|V_{MT}/v^*_{motor}|$), which we termed "efficiency ratio," as it represents how much of the motor activity is converted into MT movement and is comprised between 0 and 1. A value close to 0 corresponds to a situation where the motor activity is mostly converted into bead movement, with little MT motion, much like a vesicle trafficking on a static MT network. Conversely, a value close to 1 corresponds to a large MT motion, and little bead motion, mimicking MT outward transport [10, 11, 15]. By plotting this efficiency ratio, as a function of L_{MT}/R_{bead}, for all bead and MT sizes, we found that our experimental conditions covered nearly all values of efficiency (Figure 2D). Importantly, the efficiency ratio depends on L_{MT}/R_{bead} and not on R_{bead} itself. To compare our data with a simple theoretical situation, we computed this curve assuming the medium was a Newtonian fluid and neglected potential effects, such as the hydrodynamic coupling between the bead and the MT or the rotation of the bead as it moves along the MT (STAR Methods). We find that our data are systematically above this theoretical curve but follow the same trend (Figure 2D). In fact, our data can be well fitted by the same theoretical formula, with a 2.4-fold reduction of the MT drag coefficient relative to the bead drag coefficient (Figure 2D; STAR Methods). This reduction of the effective MT drag coefficient favors its movement and could be caused by the non-Newtonian nature of the medium and an effect known as "shear thinning," where the MC polymers in the medium would be locally stretched along the highly anisotropic MT shape, thereby reducing its viscous friction as it moves [30, 31]. Alternatively, this effect could also be caused by scale-dependent viscosity, when the size of the object (here the radius of the MT) approaches the mesh size of the polymer solution [32].

Collective Effects of Multiple Cargos Pulling on MTs and Minimal "Asters"

To tackle another physiologically relevant situation where more than one cargo is applying bulk forces to a MT, we investigated the collective effect of several beads moving on a MT. Such experiments are relevant to aster centration, where it has been proposed that longer MTs could accumulate more cargos, thereby applying larger forces to centrosomes [8, 9, 17]. Given that, in our bulk motility assay, the number of events where two beads encounter a MT naturally was very low, we used an optical trap to place two beads on the MT (Figure 3A; Video S2). We observed that MTs with two beads moving along them were displaced more rapidly than MTs of comparable length with only one bead (Figure 3B and Video S3 show an example of this general observation). Consistently, the movement of a MT with two mobile beads slowed down when one bead reached the MT minus end and stopped (Figure S3B). Data points obtained with 2 beads were also in the vicinity of the master curve of Figure 2D, considering the average motor speed and the sum of the bead radii (Figure 3C; STAR Methods). Importantly, we did not notice any obvious slowdown of MT speed, even when beads were moving close to each other, suggesting that putative hydrodynamic screening between cargos does not significantly affect force additivity (Figure S3C). These data show that the forces exerted by multiple cargos are additive, providing an *in vitro* validation that longer MTs with more cargos may be pulled more.

We next investigated another important situation where these forces could pull in different directions, generating a tug-of-war. To do so, we built artificial, minimal asters, consisting of two or three MTs. These minimal asters were built using dynein-coated beads and the optical trap. Briefly, we first placed a bead on a MT, let it reach and stop at the minus end, and repeated this operation with the same bead on another MT (Figure S3D; STAR Methods). This resulted in a construction made of two or three MTs, with their minus ends bound to a single bead that we refer to as the "aster center." Using the optical trap, we then placed two or three other beads on MTs, near their plus ends, and tracked their movements as well as the concomitant movement of the aster center (Figure 4). This assay thus allows to reconstitute the basic elements of more complex *in vivo*

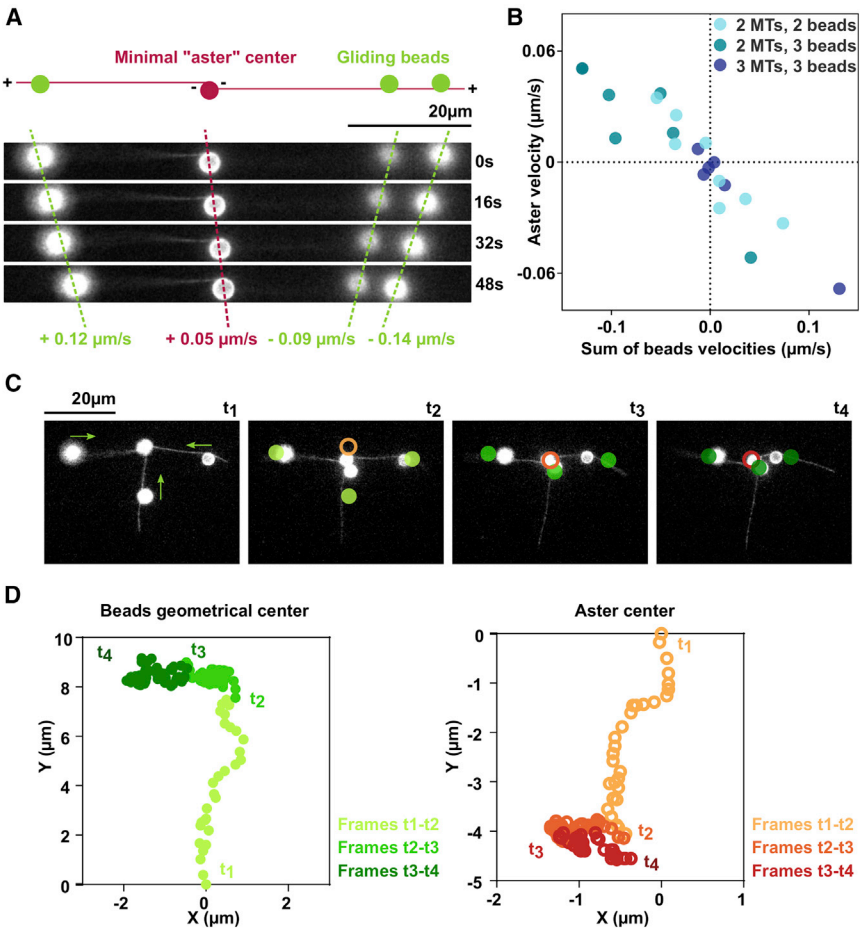

Figure 4. Beads Pulling on MTs in Bulk Can Move a Minimal "Aster" in 2D

(A) Time lapse of three dynein-coated beads gliding on a minimal aster composed of two anti-parallel MTs bound together by a dynein-coated bead at their minus ends (red), which is immobile relative to the MTs.

(B) Aster center velocity plotted as a function of the sum of dynein-coated gliding beads' velocities for tugs-of-war between two or three motile beads walking on a two-MT minimal aster or three motile beads walking on a three-MT minimal aster (n = 20, 10 independent experiments, two protein batches).

(C) Time lapse showing three dynein-coated beads pulling on a minimal aster made of 3 MTs (3-µm beads in a 39-cP MC viscous medium). In each image, the positions of the walking beads from the previous image are shown as plain circles, and the position of the bead marking the "aster center" from the previous image is shown as a hollow circle.

(D) Positions of the geometrical centers of the dynein-coated beads gliding along MTs and of the aster center computed from the time lapse shown in (C).

See also Figures S3 and S4 and Video S4.

situations, where several objects pull on several MTs, for example, when organelles pull on front versus back MTs of a centering aster [6].

Minimal asters made of two aligned, antiparallel MTs provided a tug-of-war situation (Figure 4A; Video S4), illustrating that a minimal aster will move toward the region where more cargos are being transported. Following a hydrodynamic force balance, the velocities of different minimal asters were here also dictated by the vectorial sum of cargo velocities (Figure 4B). To further illustrate the generalization of this principle to more complex bi-dimensional asters, we also tracked the 2D movement of a minimal aster made of three MTs and three motile beads (Figures 4C and 4D; Video S4). As above, we could detect that the movement of the aster center globally followed the 2D direction and amplitude, set by the vectorial sum of motile cargo velocities. We thus showed that cargos gliding on MTs of a minimal aster will displace this aster in the direction set by the vectorial sum of the hydrodynamic forces exerted on these objects, with a speed scaled to the net sum of cargo speeds.

DISCUSSION

We here report on the development of a minimal bulk motility assay to study and evidence the role of bulk motor forces on MTs. This assay shows that a mobile cargo moving along a MT exerts a force on that MT from within the viscous medium, which is sufficient to displace the MT over long distances of tens of µm. The forces exerted by multiple cargos on a MT add up and are expected to reach the pN range, comparable to other typical forces applied to MTs in cells. By spanning bead sizes and MT lengths, we reproduce a range of physiologically relevant behaviors, from bare centripetal trafficking to MT outward propulsion reported in many cells. Reconstituted tugs-of-war show that minimal asters will move toward the region where more cargos are being transported, essentially recapitulating models proposed *in vivo*, for aster self-propelling motions that follow the direction of asymmetries in MT lengths and/or bulk cargo densities [6, 8, 9, 17].

In our assay, cargos with all types of directionalities and sizes may effectively apply forces to move MTs. However, the important question of which specific cargos effectively promote aster centration in cells remains mostly open, although specific types of trafficking vesicles have been proposed in some systems [6, 12, 13]. Large cargos, like the endomembrane networks of the endoplasmic reticulum, may have higher effective drag coefficients but also require more motors to be pulled at the same speed than small cargos. The efficiency of cargo-based bulk pulling for a dense MT aster network is also predicted to be affected by the surrounding MTs in the aster, because of the putative complex hydrodynamic interactions between cargos and neighboring MTs [33]. As an evidence for this, a simple assay using our optical trap shows that the motion of a non-coated bead close to a free MT can move the MT with a speed of up to ~20% of the bead speed (Figures S4A–S4C). In a dense aster, we speculate that this effect may become more important, plausibly

limiting force transmission from cargos to MT asters. Our assay also indicates that the non-Newtonian nature and shear-thinning properties of a dilute polymeric solution, or mesh-size effects, could significantly reduce the longitudinal drag coefficient of MTs, thereby facilitating their displacement over that of cargos. These results may have direct relevance to the cytoplasm, which is a complex non-Newtonian fluid filled with polymers and membranes and which also exhibits shear-thinning properties and a scale-dependent viscosity [34, 35]. Minimal *in vitro* MT force generation assays have paved the way to our understanding of the role of MT forces in cells [3, 36]. We foresee that further complexification of this minimal bulk motility assay, potentially incorporating complex fluids closer to the cytoplasm, cytoskeletal networks, or more physiological groups of active motors, including the full dynein-dynactin adaptor complex, will serve to decipher the key physical and biological elements promoting and limiting bulk dynein hydrodynamic force exertion in cells.

STAR★METHODS

Detailed methods are provided in the online version of this paper and include the following:

- KEY RESOURCES TABLE
- RESOURCE AVAILABILITY
  - Lead Contact
  - Materials Availability
  - Data and Code Availability
- EXPERIMENTAL MODEL AND SUBJECT DETAILS
- METHOD DETAILS
  - Proteins expression and purification
  - Buffers
  - Microscopy chambers
  - Microscopy experiments
  - Acquisition
- QUANTIFICATION AND STATISTICAL ANALYSIS
  - Specific experiments and analysis
  - Classical gliding assay and bead gliding assay
  - Bulk motility assay: beads motion on one MT
  - Bulk motility assay: beads motion on a minimal aster
  - MSD measurement for viscosity assessment
  - Relation between speed and dimension of MT and beads
  - Hydrodynamic interaction experiment (Figure S4)

SUPPLEMENTAL INFORMATION

Supplemental Information can be found online at https://doi.org/10.1016/j.cub.2020.08.078.

ACKNOWLEDGMENTS

We gratefully thank Carsten Janke from Curie-Orsay for providing us with porcine brain tubulin and the mouse kinesin plasmid. We also thank Bérengère Guichard for her valuable technical help, Dmitry Ershov and Serge Dmitrieff for their help with software and statistical analysis, and all the members of the teams "Cellular spatial organization" and "Regulation of actin assembly dynamics" for fruitful discussions. We also thank our colleagues A. Guichet, J. Heuvingh, and O. Du Roure for carefully reading the manuscript. This work was supported by the Centre National de la Recherche Scientifique (CNRS), the European Research Council (ERC CoG Forcaster no. 647073) to N.M. and (ERC StG BundleForce no. 679116) to A.J., and Japan Society for the Promotion of Science KAKENHI (18K06147 and 19H05379) to T.S. H.P. acknowledges the "École Doctorale FIRE - Program Bettencourt" and a fellowship from the "Fondation pour la Recherche Médicale" (FRM) (FDT201904008226).

AUTHOR CONTRIBUTIONS

Conceptualization, N.M., G.R.-L., A.J., and H.P.; Methodology, T.S., J.S., B.L., and H.P.; Investigation, N.M., G.R.-L., A.J., K.M., T.S., J.S., B.L., and H.P.; Writing – Original Draft, N.M., G.R.-L., and H.P.; Draft Editing, N.M., G.R.-L., A.J., K.M., T.S., J.S., B.L., and H.P.

DECLARATION OF INTERESTS

The authors declare no competing interests.

Received: May 4, 2020
Revised: August 3, 2020
Accepted: August 24, 2020
Published: September 17, 2020

REFERENCES

1. Dogterom, M., Kerssemakers, J.W.J., Romet-Lemonne, G., and Janson, M.E. (2005). Force generation by dynamic microtubules. Curr. Opin. Cell Biol. *17*, 67–74.
2. J. Howard, ed. (2001). Mechanics of Motor Proteins and the Cytoskeleton (Sinauer Associates).
3. Laan, L., Pavin, N., Husson, J., Romet-Lemonne, G., van Duijn, M., López, M.P., Vale, R.D., Jülicher, F., Reck-Peterson, S.L., and Dogterom, M. (2012). Cortical dynein controls microtubule dynamics to generate pulling forces that position microtubule asters. Cell *148*, 502–514.
4. Grill, S.W., Gönczy, P., Stelzer, E.H., and Hyman, A.A. (2001). Polarity controls forces governing asymmetric spindle positioning in the Caenorhabditis elegans embryo. Nature *409*, 630–633.
5. Hamaguchi, M.S., Hamaguchi, Y., and Hiramoto, Y. (1986). Microinjected polystyrene beads move along astral rays in sand dollar eggs. Dev. Growth Differ. *28*, 461–470.
6. Kimura, K., and Kimura, A. (2011). Intracellular organelles mediate cytoplasmic pulling force for centrosome centration in the Caenorhabditis elegans early embryo. Proc. Natl. Acad. Sci. USA *108*, 137–142.
7. Minc, N., Burgess, D., and Chang, F. (2011). Influence of cell geometry on division-plane positioning. Cell *144*, 414–426.
8. Tanimoto, H., Kimura, A., and Minc, N. (2016). Shape-motion relationships of centering microtubule asters. J. Cell Biol. *212*, 777–787.
9. Wühr, M., Tan, E.S., Parker, S.K., Detrich, H.W., 3rd, and Mitchison, T.J. (2010). A model for cleavage plane determination in early amphibian and fish embryos. Curr. Biol. *20*, 2040–2045.
10. Ishihara, K., Nguyen, P.A., Groen, A.C., Field, C.M., and Mitchison, T.J. (2014). Microtubule nucleation remote from centrosomes may explain how asters span large cells. Proc. Natl. Acad. Sci. USA *111*, 17715–17722.
11. Cheng, X., and Ferrell, J.E., Jr. (2019). Spontaneous emergence of cell-like organization in *Xenopus* egg extracts. Science *366*, 631–637.
12. Xie, J., and Minc, N. (2020). Cytoskeleton force exertion in bulk cytoplasm. Front. Cell Dev. Biol. *8*, 69.
13. Barbosa, D.J., Duro, J., Prevo, B., Cheerambathur, D.K., Carvalho, A.X., and Gassmann, R. (2017). Dynactin binding to tyrosinated microtubules promotes centrosome centration in C. elegans by enhancing dynein-mediated organelle transport. PLoS Genet. *13*, e1006941.
14. De Simone, A., Spahr, A., Busso, C., and Gönczy, P. (2018). Uncovering the balance of forces driving microtubule aster migration in C. elegans zygotes. Nat. Commun. *9*, 938.
15. Keating, T.J., Peloquin, J.G., Rodionov, V.I., Momcilovic, D., and Borisy, G.G. (1997). Microtubule release from the centrosome. Proc. Natl. Acad. Sci. USA *94*, 5078–5083.

16. Hamaguchi, M.S., and Hiramoto, Y. (1986). Analysis of the role of astral rays in pronuclear migration in sand dollar eggs by the colcemid-UV method. Dev. Growth Differ. *28*, 143–156.

17. Kimura, A., and Onami, S. (2005). Computer simulations and image processing reveal length-dependent pulling force as the primary mechanism for C. elegans male pronuclear migration. Dev. Cell *8*, 765–775.

18. Pierre, A., Sallé, J., Wühr, M., and Minc, N. (2016). Generic theoretical models to predict division patterns of cleaving embryos. Dev. Cell *39*, 667–682.

19. Longoria, R.A., and Shubeita, G.T. (2013). Cargo transport by cytoplasmic dynein can center embryonic centrosomes. PLoS ONE *8*, e67710.

20. Delatour, V., Helfer, E., Didry, D., Lê, K.H.D., Gaucher, J.-F., Carlier, M.-F., and Romet-Lemonne, G. (2008). Arp2/3 controls the motile behavior of N-WASP-functionalized GUVs and modulates N-WASP surface distribution by mediating transient links with actin filaments. Biophys. J. *94*, 4890–4905.

21. Numata, N., Shima, T., Ohkura, R., Kon, T., and Sutoh, K. (2011). C-sequence of the dictyostelium cytoplasmic dynein participates in processivity modulation. FEBS Lett. *585*, 1185–1190.

22. Imai, H., Shima, T., Sutoh, K., Walker, M.L., Knight, P.J., Kon, T., and Burgess, S.A. (2015). Direct observation shows superposition and large scale flexibility within cytoplasmic dynein motors moving along microtubules. Nat. Commun. *6*, 8179.

23. Shimizu, T., and Katsura, T. (1988). Steady-state kinetic study on the inhibition of the adenosinetriphosphatase activity of dynein from Tetrahymena cilia by glycerol. J. Biochem. *103*, 99–105.

24. Terashita, S., Kato, T., and Sato, H. (1983). Reaction mechanism of 21S dynein ATPase from sea urchin sperm. I. Kinetic properties in the steady state. J. Biochem. *93*, 1567–1574.

25. Happel, J., and Brenner, H. (2012). Low Reynolds Number Hydrodynamics: With Special Applications to Particulate Media*Volume 1* (Springer Science & Business Media).

26. Hunt, A.J., Gittes, F., and Howard, J. (1994). The force exerted by a single kinesin molecule against a viscous load. Biophys J. *67*, 766–781.

27. Hiramoto, Y. (1969). Mechanical properties of the protoplasm of the sea urchin egg. II. Fertilized egg. Exp. Cell Res. *56*, 209–218.

28. Rai, A.K., Rai, A., Ramaiya, A.J., Jha, R., and Mallik, R. (2013). Molecular adaptations allow dynein to generate large collective forces inside cells. Cell *152*, 172–182.

29. Grill, S.W., Howard, J., Schäffer, E., Stelzer, E.H., and Hyman, A.A. (2003). The distribution of active force generators controls mitotic spindle position. Science *301*, 518–521.

30. Tomioka, M., and Matsumura, G. (1987). Effects of concentration and degree of polymerization on the rheological properties of methylcellulose aqueous solution. Chem. Pharm. Bull. (Tokyo) *35*, 2510–2518.

31. Chhabra, R.P., Rami, K., and Uhlherr, P.H.T. (2001). Drag on cylinders in shear thinning viscoelastic liquids. Chem. Eng. Sci. *56*, 2221–2227.

32. Brochard Wyart, F., and de Gennes, P.G. (2000). Viscosity at small scales in polymer melts. Eur. Phys. J. E *1*, 93–97.

33. Nazockdast, E., Rahimian, A., Needleman, D., and Shelley, M. (2017). Cytoplasmic flows as signatures for the mechanics of mitotic positioning. Mol. Biol. Cell *28*, 3261–3270.

34. Tsai, M.A., Frank, R.S., and Waugh, R.E. (1993). Passive mechanical behavior of human neutrophils: power-law fluid. Biophys. J. *65*, 2078–2088.

35. Luby-Phelps, K. (2013). The physical chemistry of cytoplasm and its influence on cell function: an update. Mol. Biol. Cell *24*, 2593–2596.

36. Dogterom, M., and Yurke, B. (1997). Measurement of the force-velocity relation for growing microtubules. Science *278*, 856–860.

37. Nishiura, M., Kon, T., Shiroguchi, K., Ohkura, R., Shima, T., Toyoshima, Y.Y., and Sutoh, K. (2004). A single-headed recombinant fragment of dictyostelium cytoplasmic dynein can drive the robust sliding of microtubules. J. Biol. Chem. *279*, 22799–22802.

38. Shima, T., Imamula, K., Kon, T., Ohkura, R., and Sutoh, K. (2006). Head-head coordination is required for the processive motion of cytoplasmic dynein, an AAA+ molecular motor. J. Struct. Biol. *156*, 182–189.

39. Kon, T., Shima, T., and Sutoh, K. (2009). Protein engineering approaches to study the dynein mechanism using a dictyostelium expression system. In Methods in Cell Biology, *Volume 92*, S.M. King, and G.J. Pazour, eds. (Academic), pp. 65–82, Chapter 5.

40. Castoldi, M., and Popov, A.V. (2003). Purification of brain tubulin through two cycles of polymerization-depolymerization in a high-molarity buffer. Protein Expr. Purif. *32*, 83–88.

41. Hyman, A.A. (1991). Preparation of marked microtubules for the assay of the polarity of microtubule-based motors by fluorescence. J. Cell Sci. *1991*, 125–127.

STAR★METHODS

KEY RESOURCES TABLE

REAGENT or RESOURCE	SOURCE	IDENTIFIER
Bacterial and Virus Strains		
Rosetta (DE3)pLysS E.coli	Sigma-Aldrich	71401
MB35-integrated *Dictyostelium discoideum*	[37]	IK40
Biological Samples		
Pig brain tubulin	Carsten Janke lab, Curie Orsay	N/A
Chemicals, Peptides, and Recombinant Proteins		
ATTO-565 NHS-ester	ATTO-TEC GmbH	AD 565-35
ATTO-565-biotin	Sigma-Aldrich	92637
Methylcellulose (MC41000)	Sigma-Aldrich	M0262
Glycerol	VWR Chemicals	24388.295
Sucrose	VWR Chemicals	27480.294
Polyethylene Glycol (PEG 20000)	Sigma-Aldrich	95172
Docetaxel	Sigma-Aldrich	1885
Glutamate	Sigma-Aldrich	G1251
MES (4-Morpholineethanesulfonic acid)	Sigma-Aldrich	M8250
PIPES (1,4-Piperazinediethanesulfonic acid)	Sigma-Aldrich	P6757
MgCl2	Sigma-Aldrich	M2670
ATP (Adenosine 5′-triphosphate)	Sigma-Aldrich	A2383
GTP	Sigma-Aldrich	G8877
HEPES	Sigma-Aldrich	H3375
EGTA	Sigma-Aldrich	E3889
DTT	Euromedex	EU0006-D
MgSO4 (Magnesium sulfate)	Sigma-Aldrich	208094
CH3COOK (potassium acetate)	Prolabo	26667.293
Tris (Tris(hydroxymethyl)aminomethane)	Euromedex	200923-A
EDTA	Euromedex	EU0007-C
Leupeptin	Sigma-Aldrich	L2884
PMSF	Roche	10837091001
Chymostatin	Sigma-Aldrich	C7268
Pepstatin	Sigma-Aldrich	P5318
Mercaptoethanol	Sigma-Aldrich	M6250
ATP-Mg	Sigma-Aldrich	A9187
Imidazole	Merck	1.04716.1000
KH2PO4	Sigma-Aldrich	P0662
K2HPO4	Sigma-Aldrich	P3786
NaCl	VWR Chemicals	27810.295
KCl	VWR Chemicals	26668.296
NaH2PO4	Sigma-Aldrich	71505
NaHCO3	VWR Chemicals	27775
Biotin	Sigma-Aldrich	B4501
Blasticidin	Sigma-Aldrich	15205
G418	Sigma-Aldrich	A1720
Tetracycline	Sigma-Aldrich	87128
Kanamicin	Euromedex	UK0010-D
Chloramphenicol	Euromedex	3886-C

(*Continued on next page*)

Continued

REAGENT or RESOURCE	SOURCE	IDENTIFIER
FLAG	Sigma-Aldrich	F3290
Recombinant DNA		
HFB380 dynein heavy chain from *Dictyostelium discoideum*	[38]	N/A
HFB380 GST SNAP2 dynein heavy chain from *Dictyostelium discoideum*	[21]	N/A
Mouse kinesin (pET28-mKif5B_N1665)	Carsten Janke lab, Curie Orsay	Uniprot: Q61768
Software and Algorithms		
MATLAB R2016b	MathWorks	https://fr.mathworks.com
GraphPad Prism 6	GraphPad	http://www.graphpad.com
Other		
Ni-NTA agarose beads	Invitrogen	R901-15
Anti-FLAG beads	Sigma	F2426
NAP-5 column	GE Healthcare	17-0853-01
0,5μm beads Bangs (streptavidin coated)	Bangs laboratory	CP01F
1μm beads Bangs (streptavidin coated)	Bangs laboratory	CP01F
1μm beads Dynabeads (streptavidin coated)	ThermoFisher	65001
1,9μm beads Bangs (streptavidin coated)	Polysciences	24160
2,2μm beads Bangs YG (biotin coated)	Polysciences	24173
2,8μm beads Dynabeads (streptavidin coated)	ThermoFisher	65305
3μm beads Bangs (streptavidin coated)	Bangs laboratory	CP01N
HL5 medium	Formedium	HLF2
LoBind eppendorf microcentrifuge tubes 0,5mL	Sigma	Z666491

RESOURCE AVAILABILITY

Lead Contact

Further information and requests for resources and reagents should be directed to and will be fulfilled by the lead contact, Nicolas Minc (nicolas.minc@ijm.fr).

Materials Availability

This study did not generate new unique reagents.

Data and Code Availability

This study did not generate code. Data obtained in the current study are available from the lead contact on request.

EXPERIMENTAL MODEL AND SUBJECT DETAILS

Recombinant kinesin was expressed in Rosetta (DE3)pLysS E.coli (grown at 37°C and induced for protein production at 20°C). Recombinant dynein was expressed in IK40 MB35-integrated *Dictyostelium discoideum* (growth and protein production at 21°C).

METHOD DETAILS

Proteins expression and purification

Dynein

Recombinant cytoplasmic dynein was expressed in *Dictyostelium discoideum*, and purified following the protocol described by T. Kon et al. [39] with some modifications. This HFB380 380 kDa recombinant dynein was engineered from the *Dictyostelium discoideum* cytoplasmic dynein heavy chain gene as described previously [21]. Affinity tags were added (His6 and FLAG) at the N terminus as well as a N-terminal BioEase tag for *in vivo* biotinylation. Glutathione S-transferase (GST) could also be added for dynein dimerization. Monomeric dynein was used in the experiments involving 1μm Dynabeads (1.60% MC) and 2.8μm Dynabeads (1.18% MC), and GST dimerized dynein was used for all other conditions. Finally, a MB35 plasmid (ID 44 - Dicty Stock Center) encoding a tetracycline-controlled transcriptional activator was introduced in order to control the recombinant protein overexpression.

Cells were cultivated at 21°C in culture dishes in HL-5 medium supplemented with 10μg/mL G418 and 10μg/mL tetracycline until they reached confluence, and were then transformed through electroporation with an MB38-based plasmid containing the engineered dynein gene. 10μg/mL blasticidin was added for plasmid selection one day after electroporation. 200mL of HL5 supplemented with G418, tetracycline and blasticidine were inoculated in a confluent 10cm culture dish, and cultivated at 21°C, 200rpm. After cells had reached 10^7 cells/mL, dynein expression was induced through removal of tetracycline (centrifugation: 1,000 g, 5min, 21°C), and resuspension in 400mL HL-5 supplemented only with G418 and 20μM of d-biotin for dynein biotinylation.

Cells were harvested by centrifugation (5,000 g, 5min, 2°C), washed in 20mL lysis buffer (100 mM PIPES-KOH, 4 mM $MgCl_2$, 0.1 mM EGTA, 0.9 M glycerol, 10 mM imidazole, pH 7.0), and resuspended in an equal volume of lysis buffer supplemented with 1 mM TCEP, 10 mM ABESF, 0.2 mM leupeptin, 87 μM pepstatin, 10 mM TAME and 0.1 mM ATP. Cells were sonicated (six pulses of 3 s with 30 s pause between each pulses) and the supernatant was collected after two successive centrifugations (18,000 g, 20min, 2°C and 100,000 g, 15min, 2°C) for clarification of the lysate. This lysate was gently mixed with 300 μL of pre equilibrated Ni-NTA agarose for 1h at 4°C on a rotating wheel. The mixture was loaded on a column, column flow though was discarded, and 12 column volumes (CV) of wash buffer (100mM PIPES, 4mM $MgCl_2$, 0.1mM EGTA, 0.9M glycerol, 20mM imidazole, 1 mM TCEP, 10 mM ABESF, 0.2 mM leupeptin, 87 μM pepstatin, 10 mM TAME and 0.1mM ATP, pH 7.0) were flowed in and discarded. Bound proteins were then eluted with 2CV of elution buffer (100mM PIPES, 4mM $MgCl_2$, 0.1mM EGTA, 0.9M glycerol, 250mM imidazole, 1 mM TCEP, 10 mM ABESF, 0.2 mM leupeptin, 87 μM pepstatin, 10 mM TAME and 0.1mM ATP, pH 7.0). The eluate was supplemented with 150mM NaCl, 5mM EGTA and 0.1mM EDTA, and then gently mixed with 100 μL of pre equilibrated AntiFLAG gel for two hours at 4°C on a rotating wheel. The gel was loaded on a column, column flow through was discarded, and the gel was washed with 10CV of PMEGS buffer (100mM PIPES, 4mM $MgCl_2$, 5mM EGTA, 0.1mM EDTA, 0.9M glycerol, 200mM NaCl, 1 mM TCEP, 10 mM ABESF, 0.2 mM leupeptin, 87 μM pepstatin, 10 mM TAME and 0.1mM ATP, pH 7) and then 10CV of PMEG30 buffer (30mM PIPES, 4mM $MgCl_2$, 5mM EGTA, 0.1mM EDTA, 0.9M glycerol, 1 mM TCEP, 10 mM ABESF, 0.2 mM leupeptin, 87 μM pepstatin, 10 mM TAME, 20% (w/v) trehalose and 0.1mM ATP, pH 7.0). Bound recombinant dynein was eluted slowly with 3CV of PMEG30 buffer supplemented with 0.25mg/mL FLAG peptide. The final eluate was concentrated using Amicon Ultra-0.5mL filter, flash frozen using liquid nitrogen, and stored at −80°C. Protein concentration was determined using A_{280} or Bradford reagent with bovine serum albumin as a standard.

Kinesin

His-tagged recombinant kinesin (pET28-mKif5B_N1665, mouse kinesin N-terminal, with motor domain and coiled coil) was expressed in Rosetta (DE3) pLysS E.coli. One liter of 2YT media supplemented with 34μg/mL chloramphenicol and 50μg/mL kanamycin was grown at 37°C, 200 rpm until the OD_{600nm} was between 0.8 and 1 and transferred to 20°C. Protein expression was then induced for 4-5h at 20°C by addition of 0.5 mM IPTG. Cells were harvested by centrifugation (8,000 g, 20min, 20°C), and the pellet was resuspended in 40mL of lysis buffer (20 mM potassium phosphate, 150 mM NaCl, 10% glycerol (w/v), 5mM β-mercaptoethanol, 1mM MgCl2, 0.1mM ATP.). Cells were then sonicated (5 pulses of 15 s, 50% intensity, 6mm probe), and the lysate was clarified by centrifugation (80,000 g, 50min, 4°C). The supernatant was then mixed with 0.250mL Ni-NTA beads (pre equilibrated in equilibration buffer: 50 mM potassium phosphate, 100mM NaCl, pH 7) and incubated for 1h at 4°C under gentle agitation. The resin was washed with minimum 5CV of wash buffer (50mM potassium phosphate, 10% glycerol, 2mM β-mercaptoethanol, 25mM imidazole and 1M NaCl, pH 7) and the kinesin was eluted with 1CV of elution buffer (150mM imidazole, 50mM KCl, 10% glycerol and 10mM β-mercaptoethanol, pH 7). The eluate was dialyzed against 50 mM MOPS, 250mM NaCl, 5mM β-mercaptoethanol and 20% glycerol using a NAP-5 column (GE Healthcare), flash frozen using liquid nitrogen, and stored at −80°C. Protein concentration was determined using Bradford reagent.

Tubulin purification and labeling

Tubulin was purified from pig brains following the protocol described by Castoldi and Popov, based on cycles of polymerization and depolymerization and high-molarity buffer removal of associated proteins [40]. Fresh pig brain tissues were homogenized in 1 volume (1ml/g) of DB buffer (50mM MES pH 6.6, 1mM $CaCl_2$) and centrifuged at 29,000 g for 1h at 4°C. The supernatant was supplemented with 1 volume of high-molarity PIPES buffer (HMPB: 1M PIPES pH 6.8, 10mM $MgCl_2$, 20 mM EGTA) and 1 volume of glycerol and raised to a final concentration of 1.5mM ATP and 0.5mM GTP. The mixture was then incubated for 1h at 37°C to induce tubulin polymerization. After centrifugation at 150,000 g for 30 min at 37°C, the pellet was resuspended in 0.3 volumes of cold DB buffer and incubated for 30 min at 4°C to depolymerize microtubules. After centrifugation at 4°C for 30 min at 120,000 g, the supernatant containing free soluble tubulin was polymerized for a second cycle of 1h at 37°C after being supplemented as above with an equal volume of HMPB buffer, a volume of glycerol and with a final concentration of 0.5mM GTP and 1.5mM ATP. Polymerized tubulin was pelleted by centrifugation at 37°C for 30 min at 150,000 g. The pellet was resuspended in 0.01 volumes of cold BRB80 buffer (80mM PIPES, 1mM EGTA, 1mM $MgCl_2$, pH 6,8) and depolymerized for 1h at 4°C. The suspension was centrifuged for 30min at 4°C and 150,000 g. The supernatant containing pure soluble tubulin was aliquoted, frozen in liquid nitrogen and stored at −80°C.

Labeling of tubulin with NHS-ester-ATTO 565 (ATTO-TEC) was performed following the protocol described by Hyman [41]. Tubulin was first polymerized in presence of 1mM GTP and 3.5mM $MgCl_2$ and 25% glycerol (v/v) at 37°C for 1h. Microtubules were collected by centrifugation at 35°C for 40 min at 100,000 g through a cushion of 0.1M HEPES pH 8.6, 1mM $MgCl_2$, 1mM EGTA, 60% glycerol (v/v). The pellet containing microtubules was then resuspended in labeling buffer (0.1M HEPES pH 8.6, 1mM $MgCl_2$, 1mM EGTA, 40% (v/v) glycerol). The succinimidyl ester-coupled fluorophore (dissolved at 50mM in DMSO) was then added to a final concentration of 5mM and incubated 20 min at 37°C. Labeled microtubules were centrifuged through a cushion of 60% (v/v) glycerol in BRB80 for 40min at 35°C at 150,000 g. Microtubules were depolymerized for 30min at 4°C in 50mM K-Glutamate, 0.5mM $MgCl_2$, pH 7.0

(KOH). Tubulin was recovered by centrifugation at 4°C for 20 min at 150,000 g. The solution was brought to 80mM PIPES, 4mM MgCl2, 1mM GTP and another cycle of polymerization and depolymerization was performed. The final pellet was resuspended in cold BRB80, aliquoted, frozen in liquid nitrogen and stored at −80°C.

Microtubule polymerization

Tubulin and labeled tubulin (80μM total, with 7 to 20% labeling) were mixed in BRB80 with glycerol (80mM PIPES, 1mM EGTA, 1mM $MgCl_2$, 25% glycerol, pH 6,8), and centrifuged to remove possible proteins aggregates or impurities (100,000 g, 10min, 4°C). The supernatant was recovered in a microtube, 1mM GTP was added, and the mix was incubated 5min on ice, before incubation for polymerization for 45min at 37°C. A volume of BRB80 supplemented with 40μM docetaxel (taxol analog) was added to reach a concentration of 20μM docetaxel, and the mix was incubated for stabilization for 15 to 30 min (yielding more or less long MTs). The mix was centrifuged (100,000 g, 10min, 30°C), the supernatant removed, and the pellet washed smoothly with 10μL BRB80D20 (BRB80 supplemented with 20μM docetaxel). BRB80D20 was added to the pellet, to resuspend the MTs at 47,8μM by pipetting smoothly after letting the pellet hydrate for 10min. MTs were stored at RT in the dark.

Buffers

We performed experiments in a dynein assay buffer (10mM K-PIPES, 50mM potassium acetate, 4mM $MgSO_4$, 1mM EGTA, 10mM glucose, 25μM glucose oxydase, 6.4μM catalase, 1mM DTT, 0,4mg/mL casein, 40μM docetaxel, 1mM ATP, pH 7.0) supplemented with methylcellulose (MC) (Sigma). MC was previously prepared as a 2% solution as advised by the seller. Briefly, MC was added to half of the buffer volume heated to 80°C, agitated until particles were evenly dispersed, after which the remaining half of the buffer was added at 4°C. The mixture was then agitated at 4°C and until all the MC was dissolved and the solution became homogeneous. Glucose, DTT, casein, docetaxel and ATP were added after the solution cooled down to 4°C, and aliquots were stored at −20°C. Glucose oxydase, catalase and MTs were added just before experiments, to yield 0.85%, 1.18% or 1.60% MC MC.

Microscopy chambers

Chambers were made of two coverslips separated by one to three layers of parafilm. These coverslips were previously cleaned in ultrasound baths of Hellmanex 5%, KOH 2M, and absolute EtOH, or KOH 2M, demineralized H_20, and absolute EtOH (30min sonication in each solution, with H_20 rinsing in between each bath). Protein solutions were injected in the microscopy chambers with a pipet into chambers of 1.5 to 2mm in width, 50-440μm in height, and 0.5-2cm in length depending on experiments, resulting in a chamber volume of 3-8μL. The chambers were finally sealed with VALAP (an even mixture of vaseline, lanolin and paraffin).

Microscopy experiments

Control experiments: gliding assay

A classical MT gliding assay was carried out to verify the functionality of the purified dynein, following the protocol described by Kon et al. [39]. Microscope chambers were constructed as described above, with one layer of parafilm between coverslips, a width of 2mm, an internal height of ∼50μm, and a length of 2cm, resulting in a volume of ∼6μL. The microscope chamber was covered with biotinamidocaproyl BSA, streptavidin, passivated with casein, (with buffer washes after each of these steps) and covered with 7nM biotinylated dynein. Finally, dynein assay buffer, supplemented with 400nM labeled and docetaxel-stabilized MTs, was flowed in the chamber. MTs were then free to meet dyneins at the surface and glide on them.

Bead coating with dynein

Streptavidin beads were washed in the dynein assay buffer three times in Lobind microtubes (Sigma) (a wash included the mixing of beads in buffer, followed by a 2 minutes sonication, a centrifugation at 10,000 g, 4min, 4°C, and the resuspension of the pellet in buffer). Beads were then incubated with biotinylated dynein for ∼1-3h in the cold room with gentle agitation (incubation with a protein amount above the bead binding capacity). Beads used were 0.5μm (Bangs laboratory), 1μm (Bangs laboratory or Dynabeads from ThermoFisher), 2.2μm (Polysciences), 2.8μm (Dynabeads from ThermoFisher) and 3μm (Bangs laboratory). When beads were not already fluorescent, beads could be labeled with 0.001 fold the bead binding capacity with ATTO 565-biotin after the dynein coating step.

Bead coating with kinesin

Streptavidin beads were washed as above, and then, either kinesin was incubated with 1μm beads (Bangs laboratory) for a direct adsorption on them, either beads were first incubated with biotin anti-GST, washed, and then incubated with kinesin. Each incubation consisted of ∼1-3 hours of gentle agitation in a cold room, with a protein amount above the bead binding capacity, and each wash consisted of a centrifugation (10,000 g, 4min, 4°C).

Control experiments: bead gliding assay

Streptavidin beads were coated with dynein (as previously described). Microscope chambers were constructed as described above, with two layers of parafilm between the two coverslips, a width of 2mm, an internal height of ∼200μm, and a length of 0,5cm, resulting in a volume of ∼3μL. The microscope chamber was first covered with biotinamidocaproyl BSA and second with dynein-coated beads. Finally, dynein assay buffer supplemented with 400nM labeled and docetaxel-stabilized MTs, was flowed in the chamber.

Bulk motility assay experiment

The equivalent of approximately 0.005μL dynein-coated beads was centrifuged (10,000 g, 6min, 20°C), re-suspended in ∼3μL of by 0.85%, 1.18% or 1.60% MC dynein assay buffer at 20°C supplemented with 12.5-25nM stabilized labeled MTs, and flowed in a hand-made chamber (width of 2mm, internal height of ∼200μm, length of 0,5cm, resulting in a volume of ∼3μL) which was then sealed with

VALAP. We looked for events of a bead encountering a MT, focusing on MTs away from the surface (> 10μm from the surface) and almost parallel to the surface. Data were acquired for ∼1h.

Bulk motility assay with optical trapping

The protocol was similar to the bulk motility assay described above, with the only difference that we did not looked for bead encountering MTs naturally, but instead captured beads with an home-made optical trap (IPG Ytterbium Fiber Laser (Model YLD-10-LP)) and placed them directly onto the MTs. This was particularly necessary to study the movement of two beads on a MT, or to construct a minimal aster and place several beads on it.

Construction of an artificial minimal aster

Based on the protocol of the bulk motility assay with optical trapping, we increased the complexity of the *in vitro* reconstitution, and constructed a minimal artificial aster with 3μm dynein coated beads. A bead was placed on a MT, and as it walked on the MT, it revealed its polarity. The bead was detached from the MT by quickly pulling on it. This first step was repeated with 1 or 2 other MTs. The last MT handled was displaced thanks to the bead still present at its minus end, and with this bead, the other one or two MT precedently handled were captured by their minus ends. It resulted in a minimal aster, where two or three MT emanated from a 3μm bead. Two or three dynein coated beads could then be subsequently placed near the plus ends of the MTs of this minimal aster, to cause aster motion.

Beads MSD measurement for viscosity assessment

To compute the viscosity of different media, we computed the Mean Square Displacement of beads of different sizes (1μm (Dynabeads,ThermoFisher), and 2.8μm (ThermoFisher)) in different medium. For this, beads were mixed in 0.85%, 1.18% or 1.60% MC MC dynein assay buffer, and frames were acquired every 1 or 2 s for ∼1min (Figure S2F). For each movies, we let the fluid equilibrate long enough, to ensure that flows were negligible, and did not affect the analysis.

Hydrodynamic interaction experiment

Beads (1.9μm diameter, streptavidin coated) were labeled with ATTO 595-biotin, and mixed with stabilized labeled MTs in a viscous medium (1.18% MC dynein assay buffer). A single bead was captured with the optical trap, placed near a MT, and kept immobile there. The motorized stage was moved parallel to the MT, at velocities ranging from 1 to 45μm/s, resulting in a situation equivalent to the trapped bead being displaced near an immobile MT. The movement of the MT that may result from the bead displacement was measured to infer the hydrodynamic coupling between the two objects.

Acquisition

The microscopy chamber was placed on a Nikon EclipseTi or Nikon Eclipse TE2000-U inverted microscopes, using a 60x oil-immersion objective, with epifluorescence illumination. Microscopes were controlled through micromanager. The Nikon EclipseTi and Eclipse TE2000-U microscopes were illuminated with a Lumen Dynamics lamp (respectively X-Cite-Exacte and X-Cite-Series 120 Q) and movies were acquired by a Hamamatsu digital camera C11440 (respectively ORCA-Flash 4.0 and ORCA-Flash 4.0 LT plus)

QUANTIFICATION AND STATISTICAL ANALYSIS

Specific experiments and analysis

Measurements were done manually using ImageJ, and data were treated using Microsoft Office Excel, MATLAB R2016b and GraphPad Prism 6. Statistical analysis was done using GraphPad Prism 6.0 software. Linear regression slopes and intercepts for the three ranges of motor velocities (Figure S2C) were compared using the GraphPad linear regression tool to test if slopes and intercepts were significantly different. The test is equivalent to ANCOVA (analysis of covariance) and tests whether slopes are significantly different, and if they are not, also tests if the intercepts are significantly different. Here, as both p values were well above 0.05, the slopes and intercepts were not significantly different.

Classical gliding assay and bead gliding assay

In order to measure the MTs velocity on the dynein gliding assay, or the dynein-coated beads gliding assay, kymographs were constructed based on broken lines drawn along gliding MTs. Angles of MTs displacement were measured on the kymograph, and velocities were deducted from them.

Bulk motility assay: beads motion on one MT

The analysis was carried on ImageJ: events were checked for persistent movements and constant velocity on kymographs. During these constant velocity periods, thus excluding the occasional pauses of beads on MTs distances traveled by the MT and the bead were measured on the movie (as shown in Figure S1). In addition to brownian motion, moderate local fluid flows in the microchamber added some noise to our measurements. We selected MTs parallel or almost parallel to the focal plane, and verified using z stacks that we made negligible errors when measuring their length and tracking their motion in 2D. MT length was measured as the length of a broken line following the MT from its minus end to its plus end, on one frame of the movie, or, when the MT was not in perfect focus through the time-lapse, on a small z stack done after the movie. MT bundling was assessed by comparing the MT fluorescence with the one of single MTs. As shown in Figure S1D, a two pixels wide broken line was drawn along the MT, to plot the fluorescence profile,

and the fluorescence intensity of the background was subtracted to the fluorescence values. MTs bundles could then be detected, as for example, an approximately two fold increase of the fluorescence intensity was observed in the MT region where two MTs were bundled together.

Bulk motility assay: beads motion on a minimal aster

The movements of beads were tracked on ImageJ, following the bead with a circle and measuring its centroid, using a sub-sampling of 1/100th of the pixel size to increase the measurement precision. Velocities of walking beads and aster center bead could then be deduced from these positions.

MSD measurement for viscosity assessment

We selected beads in focus to be tracked, and checked that they were single beads (and not aggregates) with a z stack acquisition at the end of the movie. Beads centers were tracked with the ImageJ manual tracking tool. Mean Square Displacements (MSD) were then plotted as a function of the time, and the diffusion coefficient D was deduced from the slope of the fit.

This allowed to compute a diffusion coefficient, from the relation $2nD = (MSD / \Delta t)$, with n the number of dimensions (here $n = 2$ as we are measuring the MSD in 2D). The viscosity felt by the beads could then be calculated, using the Stokes–Einstein equation, for diffusion of spherical particles in a liquid at low Reynolds number: $\mu = (kT / 6\pi rD)$, with k the Boltzmann constant, T the temperature and r the beads radius.

Relation between speed and dimension of MT and beads

For one bead on one MT

Let us first consider a single motor-coated bead moving along a single MT, in solution, away from all surfaces. Neglecting drift and diffusion, all movements occur along the axis materialized by the MT, which we arbitrarily choose to orient toward the MT minus end. In the laboratory frame of reference, the bead and the MT move with velocities V_{bead} and V_{MT}, respectively. For the isolated system (bead + MT), the force balance yields: $\gamma_{MT} v_{MT} + \gamma_{bead} v_{bead} = 0$, where γ_{MT} and γ_{bead} are the MT longitudinal drag coefficient, and the bead drag coefficient, respectively.

Based on Stokes's law, the drag coefficient of the bead is expected to scale with the bead radius, R_{bead}. Within our range of MT lengths, we can reasonably approximate the longitudinal drag coefficient of the MT as a linear function of the MT length, L_{MT} [2, 25]. We can thus write $\gamma_{bead} = \mu \alpha_{bead} R_{bead}$ and $\gamma_{MT} = \mu \alpha_{MT} L_{MT}$, where α_{bead} and α_{MT} are geometrical constants, and μ is the viscosity of the medium. As a consequence, the speed ratio $-V_{bead}/V_{MT} = \alpha_{MT}L_{MT} / \alpha_{bead}R_{bead}$ is expected to scale with the MT-length-to-bead-radius ratio, independently of the viscosity of the medium.

In order to assess how efficiently the activity of the motor is converted into MT movement, it is convenient to compute the MT-to-motor speed ratio $-V_{MT}/v^*_{motor}$, where v^*_{motor} is the speed at which the motor transports the bead along the MT, and which can be written $v^*_{motor} = V_{bead}-V_{MT}$. Based on the previous equations, this "efficiency" ratio can be written as:

$-V_{MT}/v^*_{motor} = 1/(1+ \alpha_{MT}L_{MT} / \alpha_{bead}R_{bead})$, and is comprised between 0 and 1.

Fitting the experimental plot of $-v_{MT}/v^*_{motor}$ versus L_{MT}/R_{bead} (Figure 2E) with this equation provides an estimation of $\alpha_{MT}/\alpha_{bead}$, which is the only free parameter of the fit. We thus find this number to be 0.019, which is approximately 2.4-fold smaller than what can be computed theoretically for a Newtonian medium, based on Stokes's equation and on our linear approximation of the MT longitudinal drag coefficient (Figure S3A). This difference may be explained by the fact that the buffer supplemented with MC may behave as a non-Newtonian fluid, and thus exhibit significant shear-thinning effects [30]. In addition, our theoretical computation also neglects potential complications such as the hydrodynamic coupling between the bead and the MT, and the rotation of the bead as it moves along the MT.

For two beads moving along a single MT

Considering that the drag forces of two motile beads are independent and additive, the force balance yields $\gamma_{MT} V_{MT} + \gamma_{bead1} V_{bead1} + \gamma_{bead2} V_{bead2} = 0$, and the computation of the ratio $-V_{MT}/v^*_{motor}$ then leads to:

$-V_{MT}/ < v^*_{motor} > = 1/(1+ \alpha_{MT}L_{MT} / 2\alpha_{bead}R_{bead})$, where $< v^*_{motor} > = (v^*_{motor1}+v^*_{motor2})/2$ is the average motor speed (Figure 3C).

For multiple beads moving on a minimal aster

We now consider the movement of N motor-coated beads on a set of MTs connected by their minus ends to a central bead. Movements are observed in the focal plane of the microscope, in two dimensions. The minimal aster is thus composed of the central bead and the MTs, and has a non-isotropic drag coefficient. Balancing the drag forces yields, projected on a x axis parallel to the two MTs in the minimal aster:

$$\gamma_{x,aster} v_{x,aster} + \gamma_{bead1} v_{x,bead1} + \ldots + \gamma_{bead\ N} v_{x,bead\ N} = 0,$$

where $\gamma_{x,aster}$ is the drag coefficient of the minimal aster for movements along the x axis.

Thus $v_{x,aster}$ should scale with $-(v_{x,bead1} + \ldots + v_{x,bead\ N})$. (Figure 4B).

Hydrodynamic interaction experiment (Figure S4)

An optically trapped bead was displaced near a freely floating MT, by keeping the trapped bead in a fixed position, in the frame of reference of the microscope, while moving the entire chamber thanks to a motorized stage. A free bead, away from the MT and the

trapped bead, was used to monitor the movement of the stage, in the frame of reference of the microscope. All movements were then determined in the frame of reference of the stage, by using the free bead as a reference.

The velocity of the trapped bead was thus measured, in the frame of reference of the stage, and so was the velocity of the MT, resulting from the hydrodynamic coupling with the trapped bead displaced parallel to it. The MT-to-bead speed ratio can be plotted as a function of the MT distance from the surface of trapped bead, and data can be fitted as a power series (Figure S4C).